Dynamical Range of the WINDMI Model:
An exploration of possible magnetospheric plasma states

James P. Smith, Jean-Luc Thiffeault,[1] and Wendell Horton

Institute for Fusion Studies and Department of Physics,
University of Texas at Austin, Austin, Texas.

Short title: DYNAMICAL RANGE OF THE WINDMI MODEL

Abstract.

This paper explores the dynamical range of the WINDMI model [*Horton and Doxas,* 1998]. Such low-dimensional models provide us with the tools to understand the relationships of simple physical quantities within the magnetosphere (such as energy deposition, macroscopic currents, cross-tail voltage, etc.) without the necessity of coping with the more complete but unwieldy models (MHD or particle codes, for example). The model is highly versatile: certain regions of the parameter space support stable fixed points, while others contain periodic states that exhibit period doubling, and sometimes chaos. States in each of these regimes (stable, periodic, chaotic) are investigated for their ability to accurately describe the observed properties of the magnetosphere-ionosphere system. A brief discussion of applications of this model to current space physics problems is included.

1. Introduction

In this paper we explore the dynamical states possible in the WINDMI model of *Horton and Doxas* [1998]. The WINDMI model follows a long tradition, begun with *Lorenz* [1963] for atmospheric dynamics, of projecting a set of partial differential equations (PDEs) onto a relatively small set of moments in order to study the dynamical properties of a system. We thus obtain a finite set of ordinary differential equations, or ODEs. The idea of such low-dimensional (or low-order) models is to capture as much of the dynamical behavior of the system as possible without resorting to solving the full PDEs. Indeed, a direct solution of the PDEs often obscures the exact relationships between the different physical quantities involved. The numerical methods by which one solves PDEs directly (i.e. MHD) also involve projecting onto ODEs, but require a very large number of them. However, the direct solution of the PDEs does provide detailed spatial resolution not possible in low-order models.

The WINDMI model is derived from an analysis of the physical processes present in the magnetosphere-ionosphere system, together with careful considerations of the energy-balance relations. The resulting six ODEs provide physically meaningful values for the major energy sub-components of the global magnetosphere. The preservation of such energy relations has been shown to be important in low-order dynamical systems [*Treve and Manley,* 1982; *Thiffeault and Horton,* 1996]; it ensures, for instance, that solutions of the set of ODEs remain bounded for all times. Our low-order model has a fixed, mean configuration that forms the basis functions for the electromagnetic fields. Due to their complex shape, the usual sine and cosine basis functions (as used in the aforementioned studies) are not suitable. Instead we use the well-known distributed current systems of the magnetosphere and allow time-dependent amplitudes of these new basis functions. The formal justification for the method is given in *Padhye and Horton* [1999], based on a variation of the action of the electromagnetic particle Lagrangian that leads to the ODEs.

A model state (choice of parameters) should be able to describe the behavior observed in the ionosphere and magnetosphere. We qualitatively categorize the states possible in the WINDMI model, and assess their relationship with observations.

The report is composed as follows: Section 2 outlines the low-dimensional model and derives its dimensionless form, which expresses the relevant parameter space most succinctly. The fixed points and spectral linear stability of the system are analyzed in Section 3. In Section 4, a brief review is given of the types of nonlinear states possible, and in Section 5, a survey of the different forcing dependent model states is presented. Section 6 summarizes the principal findings.

2. The low-dimensional model

The six-dimensional nonlinear dynamics model is derived from the major energy components of the magnetosphere coupled to the night-side ionosphere through region-1 currents. The details of the derivation are not presented here, but can be found in *Horton and Doxas* [1998] or more completely in *Smith* [1999]. Part of the system is related to the Faraday loop model of *Klimas et al.* [1992]. The major components of the model are the cross tail potential drop V, the current I in the magnetotail current loop around the upper magnetospheric lobe, the region-1 current I_1, the potential V_i across the ionosphere connecting the nightside region-1 current system, the plasma pressure P in the central plasma sheet of the magnetosphere, and the parallel streaming kinetic energy $K_\parallel$ from the central plasma sheet. As derived in *Horton and Doxas* [1998], with fifteen free parameters, the model is as follows:

$$L\frac{dI}{dt} = V_{sw} - V + M\frac{dI_1}{dt} \tag{1}$$

$$C\frac{dV}{dt} = I - I_1 - I_{ps} - \Sigma V \tag{2}$$

$$\frac{3}{2}\frac{dP}{dt} = \Sigma\frac{V^2}{\Omega} - u_0 K_\parallel^{1/2}\Theta(I)P \tag{3}$$

$$\frac{dK_\parallel}{dt} = I_{ps}V - \frac{K_\parallel}{\tau_\parallel} \tag{4}$$

$$L_i\frac{dI_1}{dt} = V - V_i + M\frac{dI}{dt} \tag{5}$$

$$C_i\frac{dV_i}{dt} = I_1 - \Sigma_0 V_i \tag{6}$$

where V_{sw} is the driver, proportional to the solar wind-cross tail electric field, and

$$I_{ps} = \alpha P^{1/2} \tag{7}$$

$$\Sigma_0 = \Sigma_i + \gamma(I_1 V_i)^{1/2} \tag{8}$$

$$\Theta(I) = \frac{1}{2}\left[1 + \tanh\left(\frac{I - I_c}{\Delta I}\right)\right]. \tag{9}$$

To simplify the analysis, we assume that V_{sw} is constant and therefore one of our parameters. The parameter state is thus given by $\mu^{(15)} = \{V_{sw}, L, C, \Sigma, L_1, C_i, \Sigma_i, \gamma, M, \alpha, \Omega, u_0, I_c, \Delta I, \tau_\parallel\}$. As with the model derivation, the derivation of the model parameters from physical parameters can be found in *Horton and Doxas* [1996, 1998] and *Smith* [1999]. In general, they correspond to space averages of physical parameters in the moment equations from which the model was derived, like the volume of the plasma sheet or the ion gyroradius, or to ratios of parameters integrated over the magnetotail or the plasma sheet.

Before embarking on a study of the types of behavior this model exhibits, we will choose a judicious scaling of our dynamical variables. This has two main

benefits. The first is that we can choose the scales so that the typical magnitude of the dynamical variables are comparable. This facilitates numerical integration by eliminating unnecessary roundoff error. The second benefit is that by doing so we isolate the *dimensionless parameters* of the system, which are a more concise representation of the state of the system. With such a large parameter space, any reduction of the number of parameters is welcome.

We start by including natural scalings into each of the variables, to be determined later. So, for example, the lobe current, I, would become $S_I I'$, where S_I is the current scaling with units of $[I]$ and I' is dimensionless. The time derivative of the lobe current would likewise become $(S_I/S_t)\,dI'/dt'$. We then rewrite the equations such that all scalings and other coefficients appear on the right hand side. Relabel primed terms as un-primed, and choose four of the new coefficients to fix (in this case to one). We can eliminate four coefficients because we have four scalings, S_I, S_V, S_P, and S_t. Note that the energy scale is redundant with the time, current and voltage scales, and not a new degree of freedom, since $S_K \propto S_I S_V S_t$. Thus, from our original fifteen free parameters, we should end up with only eleven in the "essential system".

Since we are trying to equalize the differences of pressure and energy density, we set the scalings such that the coefficients in the pressure and kinetic energy equations are equal to one, except for the coefficient inside the hyperbolic tangent. From previous experience we know that the lobe current fixed point is usually just below the inversion point of the hyperbolic tangent, so we also set $S_I = I_{\mathrm{c}}$ to make the dimensionless current about one. This leaves us with the dimensionless system given by

$$\dot{I} = a_1 (V_{\mathrm{sw}} - V) + a_2 (V - V_{\mathrm{i}}) \tag{10}$$

$$\dot{V} = b_1 (I - I_1) - b_2 P^{1/2} - b_3 V \tag{11}$$

$$\dot{P} = V^2 - K_{\parallel}^{1/2} P \,\frac{1}{2}\{1 + \tanh[d_1(I-1)]\} \tag{12}$$

$$\dot{K}_{\parallel} = P^{1/2} V - K_{\parallel} \tag{13}$$

$$\dot{I}_1 = a_2 (V_{\mathrm{sw}} - V) + f_1 (V - V_{\mathrm{i}}) \tag{14}$$

$$\dot{V}_{\mathrm{i}} = g_1 I_1 - g_2 V_{\mathrm{i}} - g_3 I_1^{1/2} V_{\mathrm{i}}^{3/2} \tag{15}$$

We have combined equations 1 and 5 to eliminate the time derivatives on the right-hand side. These equations contain all of the *essential* dynamical information of the system, and we refer to them as the *dimensionless* system. The scalings that give us this system (in terms of the physical model parameters) are as follows:

$$S_t = \tau_{\parallel} \tag{16}$$

$$S_I = I_{\mathrm{c}} \tag{17}$$

$$S_K = \frac{9}{4 u_0^2 \tau_{\parallel}^2} \tag{18}$$

$$S_P = \left[\frac{3^3 \Sigma}{2^3 \Omega \alpha^2 u_0^4 \tau_\parallel^5} \right]^{1/2} \tag{19}$$

$$S_V = \left[\frac{3^5 \Omega}{2^5 \Sigma \alpha^2 u_0^4 \tau_\parallel^7} \right]^{1/4} \tag{20}$$

The relationships between the physical and dimensionless equations and coefficients are explored in more detail in the Appendix. For the dimensionless system, the state of the system is determined by the total parameter space which is now $\mu^{(11)} = \{V_{\text{sw}}, a_1, a_2, b_1, b_2, b_3, d_1, f_1, g_1, g_2, g_3\}$, including the assumed constant driving.

2.1. Sample parameter states of the model

It is not appropriate to discuss the survey of model states before first discussing attractors, stability, and fixed points. However, discussion of these topics will benefit from the use of explicit examples. We therefore give a very brief description of the four parameter states used throughout the body of this work. The model parameters defining these sample states are given in Table 1. Each of these states is an example of a class of states with certain distinguishable characteristics. An extensive study was made of the physical region of parameter space, where all parameters have physically reasonable values, and the following classes of dynamics were observed: 1) states always having one stable fixed point regardless of forcing; 2) states which are stable at low forcing and high forcing, and have a limit cycle without period doubling or chaos at mid-forcing; 3) like class (2), but having period doubling and chaos in the unstable region; and 4) unstable at low forcing, stable at high forcing. These features are all described in detail for the chosen sample states in the following sections.

2.2. Applications of the model

The WINDMI model affords the possibility of understanding truly global aspects of magnetospheric physics not possible in any other type of model in a very simple way, nor from the local, point measurements of spacecraft. Furthermore, it is very straightforward to develop a simple code implementing this model. The purpose of this report is to thoroughly detail the dynamical aspects of the model and differentiate classes of parameters, but in this section we remind the reader of the model's potential and applications.

Previous publications (in which the model was derived) demonstrated the success with which the auroral index, AL, could be predicted with this model. It was chosen for comparison because of the direct connection of the model with the region-1 current system and the fact that this is one of only a few global indices available. It is difficult to compare the model with local, point measurements because all quantities in the model are global. Because those early papers were primarily deriving the model, what

was not included was a careful analysis of the global energy pathways used during those substorms, and where and when the energy is stored throughout the event. This is the strong suit of the model—being able to directly track energy through the global magnetosphere—and work is underway to study the global energy properties of substorms using measured magnetospheric data to drive the model.

The model in its present state considers all magnetotail current physics to be projected onto the chosen distributed current systems. Work improving the model currently centers around the inclusion of two more important current systems into the "basis" set: the ring current and inner magnetosphere, and region-2 currents. It will not be necessary to actually include a ring current, but only the loss to the ring current of energy in the tail. This would allow a direct study of ring current injection from a global point of view. In its present form, we must infer ring current injection from the large amount of energy implied to leave the system on the earthward side, erroneously in the ionosphere. Preliminary work suggests that the inclusion of such a loss term would not significantly alter the dynamics presented in this paper.

The ionospheric dissipation is now modeled using the formulation of *Robinson et al.* [1988]. It would be a simple matter to exchange this for another model, and test the validity of each.

While more of an application to MHD models than for WINDMI, an interesting physics issue could be addressed by adding diagnostics to a global MHD code for the energy sub-components contained in this model which would allow direct comparison. Note that the WINDMI model contains physics beyond the MHD model in terms of a finite divergence of the heat flux and the off-diagonal momentum stress tensor.

It should be possible to estimate the dimensionless parameter values for planets with energetically significant magnetospheres, which would provide a useful perspective on the substorm/storm problem. In addition, it may be useful to ask what laboratory scale parameters could represent the Earth's geotail with time scales compared to those of electronic diagnostic equipment.

Finally, the WINDMI model could be used as an external global framework within which to evaluate the implications of the micro-instabilities of collisionless tearing modes and kinetic ballooning modes in the geotail. The threshold conditions and the growth rates of such instabilities can be used to construct a detailed parameterization of the rapid unloading parameters $(I_c, \Delta I)$ as well as influencing $\tau_\parallel$. Over one hundred articles on the details of such geotail instability theories have appeared in the past thirty years of space physics research. A central difficulty with these works has been to assess their global consequences. While there may be some attempt to embed these kinetic stability theory results in global MHD codes, this task looks difficult, even conceptually. The use of switches in the WINDMI model and its future upgrades would appear to provide a clear path for the evaluation and comparison of such local stability theory

thresholds and growth rates. Stated from another perspective, the WINDMI model may provide the method for formulating precisely the inverse problem of determining what properties the local, small scale instabilities must have to be consistent with the global electrodynamics of the driven-damped nightside magnetosphere.

3. Fixed points and linear stability

The fixed points of the system are the set of positions where the time derivatives are all zero. If the initial value is on the fixed point, the system stays there indefinitely. There are, however, two types of fixed points—stable and unstable. A stable fixed point is one where a small perturbation stays near the fixed point, while an unstable fixed point is one where a small perturbation grows exponentially away from the fixed point. Unstable fixed points are studied in more detail in Section 5.

Using Equations 10–15, the fixed points for all but the lobe current are:

$$V_0 = V_{\text{sw}} \tag{21}$$

$$V_{i0} = V_{\text{sw}} \tag{22}$$

$$I_{10} = \frac{g_3^2}{2g_1^2}V_{\text{sw}}^3 + \frac{g_2}{g_1}V_{\text{sw}} \pm \frac{g_3}{2g_1^2}V_{\text{sw}}^2\sqrt{4g_1g_2 + g_3^2V_{\text{sw}}^2} \tag{23}$$

$$P_0 = \left[\frac{V_{\text{sw}}^3}{\frac{1}{4}\{1 + \tanh[d_1(I_0 - 1)]\}^2}\right]^{2/5} \tag{24}$$

$$K_{\parallel 0} = \left[\frac{V_{\text{sw}}^4}{\frac{1}{2}\{1 + \tanh[d_1(I_0 - 1)]\}}\right]^{2/5} \tag{25}$$

The equation for the lobe current, I_0, is transcendental, and must be solved numerically. The relation between the lobe current and the forcing is:

$$I_0 - \frac{b_3}{b_1}V_{\text{sw}} - \left(\frac{g_3^2}{2g_1^2}V_{\text{sw}}^3 + \frac{g_2}{g_1}V_{\text{sw}} \pm \frac{g_3}{2g_1^2}V_{\text{sw}}^2\sqrt{4g_1g_2 + g_3^2V_{\text{sw}}^2}\right)$$
$$- \frac{b_2}{b_1}\left[\frac{V_{\text{sw}}^3}{\frac{1}{4}\{1 + \tanh[d_1(I_0 - 1)]\}^2}\right]^{1/5} = 0 \tag{26}$$

Note that there are always two fixed points of the system because of the two solutions for I_{10}, given by Equation 23. So far as we have explored, one of these roots is always unstable but does not have an independent attractor. We ignore it for the remainder of this study. The plot of the left hand side of Equation 26 is shown in Figure 1 for the parameters in state S1, listed in column 1 of Table 1, and for a forcing of $V_{\text{sw}} = 2$. (This is approximately 130 kV for state S1 and the scalings given Equations 16–20.) The root of the lobe current is where this curve crosses zero, and thus equals the left hand side of the equation. It is clear that there is one and only one root for lobe current for a given root of the ionospheric current (branch of Equation 23).

The fixed points for all of the states listed in Table 1 at a forcing of $V_{sw} = 2$ are given in Table 2. As an example of the effect of forcing on the values of the fixed point, the stable fixed point of the system for state S1 (column 1 of Table 1) is plotted versus the forcing function in Figure 2. From this can be seen that the voltage coordinates of the fixed point increases linearly with forcing, but all other variables increase faster than linearly.

It is important to note that the values of the fixed point depend on the forcing and on a subset of only seven of the ten model parameters, $\{b_1, b_2, b_3, d_1, g_1, g_2, g_3\}$. The remaining parameters, $\{a_1, a_2, f_1\}$, are not relevant to the position of the fixed point, but will determine the rate of approach to the fixed point.

The spectral stability of the system at a given fixed point is found by first linearizing about that fixed point, and then considering a perturbation of the form $e^{\lambda t}$ from the fixed point. To linearize the system we substitute for each of the variables its small deviation about the fixed point: $\mathbf{X} \rightarrow \mathbf{X}_0 + \delta\mathbf{X}$, and then keep only the terms that are of order $\delta\mathbf{X}$, using Taylor series expansion where necessary. Substituting this into Equations 10–15 and assuming the form $\delta\mathbf{X} \propto e^{\lambda t}$, we find

$$\lambda\delta I = (a_2 - a_1)\delta V - a_2\delta V_i \tag{27}$$

$$\lambda\delta V = b_1\delta I - b_1\delta I_1 - \frac{1}{2}b_2 P_0^{-1/2}\delta P - b_3\delta V \tag{28}$$

$$\lambda\delta P = 2V_0\delta V - \frac{1}{2}K_{\|0}^{1/2}\left\{1 + \tanh\left[d_1(I_0 - 1)\right]\right\}\delta P$$

$$-\frac{1}{4}K_{\|0}^{-1/2}P_0\left\{1 + \tanh\left[d_1(I_0 - 1)\right]\right\}\delta K_\|$$

$$-\frac{1}{2}K_{\|0}^{1/2}P_0\text{sech}^2\left[d_1(I_0 - 1)\right]\delta I \tag{29}$$

$$\lambda\delta K_\| = \frac{1}{2}V_0 P_0^{-1/2}\delta P + P_0^{1/2}\delta V - \delta K_\| \tag{30}$$

$$\lambda\delta I_1 = (f_1 - a_2)\delta V - f_1\delta V_i \tag{31}$$

$$\lambda\delta V_i = \left(g_1 - \frac{1}{2}g_3 I_{10}^{-1/2}V_{i0}^{3/2}\right)\delta I_1 - \left(g_2 + \frac{3}{2}g_3 I_{10}^{1/2}V_{i0}^{1/2}\right)\delta V_i, \tag{32}$$

where λ is the spectral eigenvalue and terms of order $(\delta\mathbf{X})^2$ are neglected. This is an eigenvalue problem,

$$\lambda\,\delta\mathbf{X} = \mathsf{A}\cdot\delta\mathbf{X} \tag{33}$$

where the matrix A is given by the coefficients in Equations 27 through 32, the vector $\delta\mathbf{X}$ is the perturbation array $\delta\mathbf{X} = (\delta I, \delta V, \delta P, \delta K_\|, \delta I_1, \delta V_i)$, and the eigenvalue is λ. Note that since A is real, complex eigenvalues must occur in conjugate pairs.

A *stable* fixed point is one where the real parts of all the eigenvalues ($\lambda_n, n = 1\ldots 6$) are negative—that is, the solution always decays to the fixed point (the fixed point is an *attractor*). A fixed point is unstable if the real part of at least one of the eigenvalues

is greater than zero. The system then evolves away from the fixed point, and nonlinear effects become important. For physically relevant states, the nonlinear terms must eventually saturate the instability, and the system will settle on a new attractor. A state that fails to saturate in this manner (i.e., diverges to infinity) usually indicates that the model is no longer physically relevant in that regime. Typical attractors that the system can settle on (other than fixed points) are *limit cycles*, *quasiperiodic orbits*, or *chaotic attractors*, which are explained in detail in Section 4.

Using the state S4 given in Table 1, the real and imaginary parts of the eigenvalues for a sequence of forcing values are given in Figure 3. The Hessenberg-QR algorithm was used to solve for the eigenvalues in Equation 33, and the power method for the eigenvectors. Newton–Raphson bisecton was used to solve for the fixed points. The system in this state is (spectrally) unstable at low forcing, but stable at high forcing.

4.   Review of attractors

We now discuss the different kinds of attractors on which the system can settle. We loosely define an attractor as a submanifold in phase space where the motion takes place, after initial transients have disappeared. Examples of several varieties of dynamical states are described in the present section. It is by no means an exhaustive treatment of nonlinear behavior—for that the reader should consult a more comprehensive treatise on nonlinear systems, such as the book by *Seydel* [1994] or the review by *Eckmann and Ruelle* [1985].

4.1. Fixed Points

If all of the eigenvalues of the linear analysis are negative, the attractor of the system is a fixed point, and all sufficiently nearby states decay onto that fixed point. This state was discussed in detail in Section 3. While the remaining parts of this section discuss interesting behavior on attractors, fixed points are only interesting in their decay onto the attractor. When the driving force is changing with time, this manifests itself as a kind of low-pass filter (attenuation of high-frequency modes in the Fourier transform), where the system does not move immediately onto the new fixed point for the new value of driving, but decays onto it at a characteristic rate. We call this behavior *fixed-point tracking* [*Smith,* 1999].

4.2. Limit Cycles

In a limit cycle, the variables execute periodic motion about the fixed point on a fixed orbit. But unlike a harmonic oscillator (real part of λ equals zero) where every perturbation is on its own orbit, a limit cycle has only one orbit to which all initial perturbations decay. Thus the limit cycle is a one-dimensional attractor. Regardless of

the initial condition, the system decays onto that one orbit. An example of a simple limit cycle is shown in Figure 4 in three parts. The time series shows several periods of one variable, then there is a phase plot of one variable versus another, and finally a Fourier spectrum of the first variable. In both the time series and the Fourier spectra, the system is clearly periodic. Note that in the Fourier spectrum there is very low background and sharp peaks with smooth regions in between (due to the finite resolution of the time series).

When forcing (V_{sw}) is constant, the system is said to be *autonomous* (the equations of motion do not explicitly depend on time). In that case, if the phase plot reconnects then the system is periodic. However, if forcing varies with time, the system is *nonautonomous*, and a phase plot that closes does not guarantee periodicity. It could be that the same path is followed, but the speed along the orbit changes nonperiodically.

A route often followed by chaotic systems, with respect to the variation of a bifurcation parameter, is to go from a stable fixed point to a limit cycle, and then undergo a cascade of period doublings culminating in chaos. A period doubling bifurcation occurs when, upon a change in the value of some parameters, the fundamental frequency of a limit cycle is halved. In other words, it must go around twice to return to its starting point, where it had been going around once. The orbit is still periodic, but the fundamental frequency is halved. A period doubling bifurcation of the above limit cycle (Figure 4) is shown in Figure 5.

4.3. Quasiperiodic Orbits

A limit cycle executes a single orbit and connects to itself. Another possible situation is for the system to have characteristic frequencies that are not a rational multiple of each other. If the system executes orbits on a 2-torus (the surface of a perfect donut in three dimensions), there are two frequencies involved: the toroidal frequency and the poloidal frequency. If the ratio of the frequencies is not a rational number, the orbit never connects to itself: the entire torus is covered by the orbit. This state is called *quasiperiodic*. It is often very difficult to distinguish a chaotic attractor from a quasiperiodic orbit just from looking at a time series. If the Fourier spectrum is used instead, it is clear when the signal is quasiperiodic or chaotic (compare to the chaotic spectrum in Section 4.4 below). An example of a quasiperiodic spectrum is shown in Figure 6.

4.4. Chaotic Attractors

What distinguishes a limit cycle from a chaotic attractor is that the chaotic attractor cannot be placed on a surface. The 2-torus of Section 4.3 can be mapped entirely onto a two-dimensional surface, hence its name. A chaotic attractor (continuing

to use examples in 3-space) on the other hand, while bounded (not exploring the entire 3-space), is larger than a two-dimensional surface. It is characterized by a non-integer "fractal dimension." The Lorenz attractor, for example, has fractal dimension between 2 and 3 [*Lorenz,* 1963; *Eckmann and Ruelle,* 1985]. Since the signal is inherently *not* periodic, its Fourier spectrum has a strong broadband plateau on which the periodic part of the signal resides, as depicted schematically in Figure 7. A chaotic signal is also strongly dependent on initial conditions.

5. Survey of model states

The main advantages of this model over a data-derived or empirical model is that it is based on basic physics, and the results are physically interpretable. So, for example, while it is obvious that one can easily obtain an unstable critical point by setting $a_2 > 1$, we reject this possibility: the state $a_2 > 1$ (equivalent to having the reduced mutual inductance $m > 1$ in physical parameters) is unphysical since the mutual inductance must be less than the square root of the product of the two self inductances. We are concerned only with the regions of parameter space that are physically meaningful.

In characterizing the states of the model presented here, use was made of all of the characteristics of attractors described in Section 4. No irrational tori (quasiperiodic orbits) were found, but examples of the other states are given. As mentioned, a typical state of a system can be driven into different regimes using an adjustable parameter of the system. A parameter used to cause the system to enter a different regime (as described above) is called a *bifurcation parameter.* The obvious choice in our case is to use the driving function, V_{sw}. The states presented here were chosen because the system entered several of the regimes described above in a reasonable range of forcing. But the reader should keep in mind that the system is scalable and can be driven in exactly the same state with different sets of physical parameters, if chosen to satisfy the relations in Equations A15–A19 in the Appendix. There are four free parameters in the dimensionless scaling.

The obvious place to start looking for different states is with the parameters derived from physical principles, taken from *Horton and Doxas* [1998] and shown as state S1 with the corresponding dimensionless parameters in Table 1. The next two examples are derived from the parameters in *Horton and Doxas* [1996]. They have an unstable fixed point in the middle of our forcing range of $0 < V_{sw} < 10$. These are states S2 and S3. State S2 has period doubling, but apparently no chaos, while state S3 does have a large chaotic region. The last example state is derived from S1; in state S4 the system starts in a singly periodic state whose frequency increases with forcing, and enters a small amplitude chaotic state only briefly before becoming stable for strong forcing.

5.1. S1: Fixed Point

This state has all of its parameters derived from reasonable physical estimates of the quantities they are trying to approximate, and is the only state used in *Horton and Doxas* [1998]. The distinguishing feature of this state is that it is stable independent of forcing. Conversely, most parameter sets chosen randomly have an unstable fixed point at low to medium forcing. Figure 2 shows how each of the parameters tracks with the value of the forcing function (in physical units). This is the key to understanding this state, or one like it which is globally stable. Whatever the current state of the system, it always approaches the stable fixed point. As the forcing is increased or decreased, the system tries to track the fixed point as it moves through phase space according to Figure 2. So depending on the response time of the system, which linearly is determined by the eigenvalue with the most positive real part, the system may behave in a manner that is only slightly more complicated than a low pass filter. This brings to mind the results of previous solar wind-magnetosphere coupling studies [*Smith and Horton,* 1998; *Blanchard and McPherron,* 1993], where a low pass filter model was found to adequately describe the variation observed in the AL index. Though not taking advantage of the full potential of this model, a state of this nature should be seriously considered as a candidate for magnetospheric modeling. Even in this state, one can still make use of the physical interpretation not previously available using filters.

5.2. S2: Mid-forcing period doubling

This is an example of a state with a simple limit cycle. For low values of the forcing function, the fixed point is stable. As the forcing is increased beyond 2.9, the fixed point becomes unstable and bifurcates to a singly periodic limit cycle. While the frequency of the oscillation changes with increasing forcing, the system does not bifurcate further. Above $V_{\mathrm{sw}} = 6.3$ the steady state regains stability. Figure 8 shows a bifurcation diagram generated by plotting, for each forcing level, the values of the cross-tail potential when the derivative of the cross-tail potential is zero. This includes both the positive and negative turning points (second derivative), so that if one were to plot these linearly versus forcing, the full-scale oscillation of the response to constant driving would be shown by the upper and lower bounds. However, Figure 8 is not plotted linearly because the full scale variation is much smaller than the value of the fixed point about which it oscillates and such a plot would be indistinguishable from a plot of the fixed point versus forcing. Instead, the value of the fixed point is subtracted from the values of the turning points, and the result is divided by the fourth power of the fixed point value at that level of forcing. (This scaling also exhibits more clearly the period doubling and chaos for state S3, below.) From Figure 8 it is clear where the bifurcation from a stable fixed point to a period-one oscillation occurs.

5.3. S3: Mid-forcing chaotic attractor

State S3 is rich in its properties. It is obtained by a simple one parameter modification from state S2: parameter g_3 is set to zero. It was later found that this was an extreme condition, and any value of g_3 under 3.5 was equivalent. Taking a quick glance at the value of g_3 in state S1 is even more revealing. This parameterizes the contribution of the nonlinear part of the ionospheric conductance. It is therefore interesting to note that a higher fraction of the conductance being caused by the nonlinear component of the ionospheric conductivity tends to stabilize the system.

The bifurcation diagram for S3 is shown in Figure 9, and the chaotic regions can be identified by the dense vertical bands near the middle of the forcing range. They appear so because the system is not periodic, and does not cross the $V = V_0$ plane at the same place every time around, but instead sweeps out a region of V (remember that it is still bounded). The region with an unstable fixed point occurs for $2.7 < V_{sw} < 9.6$, and is intermittently chaotic and multi-periodic for $3.9 < V_{sw} < 6.7$. A region to note is between $5.0 < V_{sw} < 5.7$, where the system goes through period halving cascades from chaos to a period five system, goes spontaneously back into chaos, then spontaneously into a period-three system, then spontaneously into period-one system. While in the period-three or period-five states, the phase diagram for the system does not change, only the frequency scale changes in the Fourier spectrum. Another feature is that in the range $5.7 < V_{sw} < 9.6$ the system undergoes a period doubling/halving cascade with only a very narrow chaotic region near $V_{sw} \sim 8.2$.

A sampling of time series, Fourier spectra, and phase diagrams for various forcing values are given in Figures 10–14. In Figure 10 it can be seen in the Fourier spectrum (note that it is plotted on a log scale here) that the time series consists only of harmonics of a fundamental frequency. The fact that the spectrum is not composed of delta functions but instead has a width to the peaks is caused by the finite sampling of the output. In Figure 11 the period doubling is unmistakable in the time series, the phase plot and the spectrum. It takes two cycles where it had previously taken only one, and the spectrum shows a growing set of peaks at the harmonics of half the fundamental frequency of Figure 10. Figure 12 shows the eventual cascade into chaos. Note that the orbit never connects in the phase plot, although it is still bounded. The spectrum is clearly not composed of a few distinct frequencies, but instead has an elevated broadband structure—so much so that the periodic structure is nearly masked in the spectrum. An example of the interesting region where a spontaneous period-three mode occurs is shown in Figure 13. The period-three structure is apparent in all three panels. The final periodic state of the system before returning to a stable fixed point is shown in Figure 14. It is a period-one state, but differs in shape and frequency from that in Figure 10.

As in state S2, it is important here to note that although the system does posses some very interesting nonlinear properties, including chaos, the peak-to-peak magnitude of that variation is never more than a few percent of the total value of the variable. This means that the primary feature of the system in this state (S3) is not the chaotic attractor, but the value of the fixed point itself. The system behaves largely the same as in state S1, where the fixed point wasn't unstable. The system tracks the fixed point, with the limit cycles and attractors accounting for only a few percent of the variation in the signal.

5.4. S4: Driven periodicity

Some of the properties of state S4 have already been explored, namely in Figure 3, showing the eigenvalues with largest real part for a sequence of forcing values. This figure can be seen to correspond to the bifurcation diagram in Figure 15, having a region from 0 to 2.1 where the fixed point is unstable. In most of that region, the system is in a limit cycle, having its period-doubling cascade and chaos compressed into a narrow region of forcing, $2.0 < V_{sw} < 2.1$, and too small to be seen in the figure.

Of course, the absence of chaos does not mean that there is nothing interesting in this state. In fact, this is a state where the full scale variation (in the region where the fixed point is unstable) is important, at least for low forcing. The variation of the amplitude of the limit cycle versus the fixed point value gradually rises from 25% at $V_{sw} = 0.05$ to about 75% at $V_{sw} = 1.5$, and then drops smoothly to zero as it approaches the point where the fixed point regains stability, at around $V_{sw} = 2.1$. This means that the chaotic region, as in the other states, does not differ appreciably from the fixed point value. However, there is a periodic (limit cycle) region at lower forcing where the system executes *large-scale* oscillations while under constant forcing.

The frequency of oscillation rises with forcing in the periodic state, from about 0.05 (one every six hours in physical units) at $V_{sw} = 0.05$ through 0.5 (one per thirty minutes) at $V_{sw} = 1.5$. Figure 16 shows the time series for the region-1 current, I_1, for four values of forcing: 0.05, 0.75, 1.5, and 2.0. The change in frequency as well as in amplitude can be seen in each panel of the figure.

These are characteristics that might be desirable. It would mean that for mild forcing, the magnetosphere-ionosphere system would produce periodic "substorms," increasing in frequency and magnitude as forcing went up. But for strong forcing, the substorms would appear to be a smaller energy pathway than the steady unloading from the "storm." This a plausible scenario for magnetosphere-ionosphere dynamics. This does not, however, mean that we must represent storms by the fixed-point-tracking behavior in this model. In all likelihood, a typical storm would be near, but not above, the threshold to stability. That would mean that most of the energy loaded into the

magnetotail is directly unloaded, but that short time-scale substorm-like unloading occurs simultaneously.

The fact that all of the states become stable at strong forcing should not be surprising—the magnetosphere in that state needs to unload its energy constantly, without time for any sort of recovery. (Of course, it is also possible that the magnetosphere is never driven so strongly.)

6. Summary

The WINDMI model is shown to have the versatility of supporting many different magnetospheric states analogous to the magnetospheric states known as: (1) the ground state, (2) steady-state convection, (3) periodic sequence of substorms [*Farrugia et al.,* 1993], (4) isolated substorms [*Blanchard and McPherron,* 1993], and (5) storms. These model states change with respect to solar wind forcing through a sequence of bifurcations. In noting the wide range of behavior observed, it should be pointed out that all of the model states presented here (S1 through S4) are relatively close to each other in parameter space. However, as with the Rayleigh–Bénard convection problem, there are scaling laws that allow a wide range of physical parameters to yield the same scaled state. This scaling suggests that other planets with strong magnetic fields may have magnetic storms and substorms not unlike those at Earth but occurring on different space-time scales.

A property possessed by the first three model states explored in this study was the tracking of the fixed point: the decay of any initial state to an attractor near, or on, the fixed point. This may correspond to steady convection at low forcing, or possibly a storm at strong forcing. For state S1, the attractor is a fixed point, and for states S2 and S3, the oscillations of the attractor about the fixed point are of negligible magnitude; thus they also track the fixed-point to a good approximation. This means that the model provides theoretical support for the heuristic arguments made in previous studies showing the applicability of low-pass filters to the solar wind–magnetosphere coupling problem. Only the fourth state presented has large-scale oscillations, but it still has the fixed point tracking property at strong forcing. This is important because it means that no matter what parameters are used in the model, the attractor at strong forcing is always a stable fixed point.

State S4 gives us a possible elucidation of the controversial current issue of the relationship between storms and substorms. Consistent with observations, we find that depending on the rate of rise of the cross tail electric field, a storm may or may not be preceded by substorms. This does *not* mean that storms are made up of substorms. Rather, it means that both storms and substorms are different facets of the same magnetospheric state (S4), depending on the strength of the solar wind forcing.

Appendix: Relationship between the physical and dimensionless models

To see how the dimensionless system relates to the physical system of equations given by the scalings in Equations 16–20, we consider some examples. First, note that a set of dimensionless parameters is unique, while a set of physical parameters has four additional parametric degrees of freedom to describe the same dynamics. Therefore our comparisons are done by fixing four of the physical parameters while matching the rest to the unique dimensionless system. Our base state for comparison, U1, is listed in the first column of Table A1 and Table A2 and consists of all dimensionless parameters equal to one except for the mutual inductance parameter, a_2. This is because there is a physical constraint on the mutual inductance,

$$M = m\sqrt{LL_1}, \qquad 0 < m < 1 \qquad (A1)$$

which does not allow us to define a dimensionless system with $a_2 = 1$ and finite corresponding physical parameters. Note that in the tables the relative mutual inductance, m, is used instead of M, the absolute mutual inductance. And keep in mind that the corresponding physical parameters are not unique. Several other states are given in the tables that display some of the relationships between the two systems of parameters, and are discussed in this section. Given the scalings chosen so that the four coefficients in the pressure and parallel energy equations go to one as described in the text, the dimensionless parameters can be related to the physical parameters using the following relations

$$a_1 = \left[\frac{3^5\Omega}{2^5\Sigma\alpha^2 u_0^4\tau_\parallel^3 I_c^4 L^4}\right]^{1/4}\frac{1}{1-m^2} \qquad (A2)$$

$$a_2 = \left[\frac{3^5\Omega}{2^5\Sigma\alpha^2 u_0^4\tau_\parallel^3 I_c^4 L^2 L_1^2}\right]^{1/4}\frac{m}{1-m^2} \qquad (A3)$$

$$b_1 = \left[\frac{2^5\Sigma\alpha^2 u_0^4\tau_\parallel^{11} I_c^4}{3^5\Omega C^4}\right]^{1/4} \qquad (A4)$$

$$b_2 = \left[\frac{2\alpha\Sigma\tau_\parallel^3}{2\Omega C^2}\right]^{1/2} \qquad (A5)$$

$$b_3 = \frac{\Sigma\tau_\parallel}{C} \qquad (A6)$$

$$d_1 = \frac{I_c}{\Delta I} \qquad (A7)$$

$$f_1 = \left[\frac{3^5\Omega}{2^5\Sigma\alpha^2 u_0^4\tau_\parallel^3 I_c^4 L_1^4}\right]^{1/4}\frac{1}{1-m^2} \qquad (A8)$$

$$g_1 = \left[\frac{2^5 \Sigma \alpha^2 u_0^4 \tau_{\|}^{11} I_c^4}{3^5 \Omega C_i^4} \right]^{1/4} \tag{A9}$$

$$g_2 = \frac{\Sigma_i \tau_{\|}}{C_i} \tag{A10}$$

$$g_3 = \left[\frac{3^5 \Omega \gamma^8 I_c^4 \tau_{\|}}{2^5 \Sigma \alpha^2 u_0^4 C_i^8} \right]^{1/8} \tag{A11}$$

In particular, it should be noted that eight of the ten dimensionless parameters have simple relationships with the physical parameters, involving only one parameter or the unique combination of two or three. The first three are:

$$d_1 = d_1(\Delta I) \tag{A12}$$

$$g_2 = g_2(\Sigma_i) \tag{A13}$$

$$g_3 = g_3(\gamma) \tag{A14}$$

while the next five are only slightly more complicated:

$$a_1 = a_1(L \mid \sqrt{LL_1}(1 - m^2)/m^2 = \text{const.}) \tag{A15}$$

$$f_1 = f_1(L_1 \mid \sqrt{LL_1}(1 - m^2)/m^2 = \text{const.}) \tag{A16}$$

$$a_2 = a_2(m \mid L(1 - m^2) = \text{const. and } L_1(1 - m^2) = \text{const.}) \tag{A17}$$

$$b_2 = b_2(\alpha \mid \alpha u_0^2 = \text{const.}) \tag{A18}$$

$$b_3 = b_3(\Sigma \mid \frac{\Sigma}{\Omega} = \text{const.}) \tag{A19}$$

Equation A17 is illustrated with examples U2 and U4. Note that in the tables, corresponding parameter changes are highlighted. So in the current examples, U2 and U4, the parameters a_2, L, L_1, and m are highlighted. State U3 demonstrates the even simpler relation in Equation A12. The last three examples explore a little of the more complicated relationships involving dimensionless parameters b_1 and g_1. State U5 shows what happens when changing only b_1 and g_1 by the same amount, while U6 and U7 show the inverse relation while changing only C or C_i. State U5 shows the complicated dependence of the physical parameters on b_1 and g_1, involving changes in nine parameters! Conversely, changing only C or C_i has an effect on three dimensionless parameters.

Also of interest are the relations between the physical system and the dimensionless system in the values of the fixed points. First we note that the parameters for the physical-parameter system corresponding to the states given in Table 1 are given in Table A3. These parameters correspond to the scalings given in Equations 16–20, and these states were discussed in detail in Section 5. The values of the fixed points of the states given in these tables are given in dimensionless units in Table 2 and in physical

units in Table A4. The equations for the fixed points in physical units in terms of physical model parameters are

$$V_0 = V_{\text{sw}} \tag{A20}$$

$$V_{\text{i0}} = V_{\text{sw}} \tag{A21}$$

$$I_{10} = \Sigma_0 V_{\text{sw}} + \frac{1}{2}\gamma^2 V_{\text{sw}}^3 \pm \frac{1}{2}\gamma V_{\text{sw}}^{3/2}\sqrt{\gamma^2 V_{\text{sw}}^3 + 4\Sigma_0 V_{\text{sw}}} \tag{A22}$$

$$P_0 = \left[\frac{\Sigma^2 V_{\text{sw}}^3}{\left[\frac{1}{2} + \frac{1}{2}\tanh\left(\frac{I_0 - I_c}{\Delta I}\right)\right]^2 u_0^2 \Omega^2 \alpha\tau}\right]^{2/5} \tag{A23}$$

$$K_0 = \left[\frac{\Sigma\alpha^2\tau^2 V_{\text{sw}}^4}{\frac{1}{2}\left[1 + \tanh\left(\frac{I_0 - I_c}{\Delta I}\right)\right] u_0 \Omega}\right]^{2/5} \tag{A24}$$

and have units of Volts (V and V_{i}), Amperes (I and I_1), Pascals (P), and Joules ($K_{\parallel}$). The equation for the lobe current fixed points is

$$0 = I_0 - \Sigma V_{\text{sw}} - \left(\frac{1}{2}\gamma^2 V_{\text{sw}}^3 + \Sigma_0 V_{\text{sw}} + \frac{1}{2}\gamma V_{\text{sw}}^{3/2}\sqrt{\gamma^2 V_{\text{sw}}^3 + 4\Sigma_0 V_{\text{sw}}}\right)$$
$$-\left(\frac{\alpha^4\Sigma^2 V_{\text{sw}}^3}{u_0^2\Omega^2\tau}\right)^{1/5}\left\{\frac{1}{2}\left[1 + \tanh\left(\frac{I_0 - I_c}{\Delta I}\right)\right]\right\}^{-2/5} \tag{A25}$$

and (still) must be solved numerically.

References

Blanchard, G. T., and R. L. McPherron, A bimodal representation of the response function relating the solar wind electric field to the AL index, *Adv. Space Res., 13*(#4), 71-74, 1993.

Clauer, C. R., R. L. McPherron, C. Searls, and M. G. Kivelson, Solar wind control of auroral zone geomagnetic activity, *Geophys. Res. Lett., 8,* 915-918, 1981.

Eckmann, J.-P., and D. Ruelle, Ergodic theory of chaos and strange attractors, *Rev. Mod. Phys., 57,* 617-656, 1985.

Farrugia, C. J., M. P. Freeman, L. F. Burlaga, R. P. Lepping, and K. Takahashi, The Earth's magnetosphere under continued forcing: Substorm activity during the passage of an interplanetary magnetic cloud, *J. Geophys. Res., 98,* 7657-7671, 1993.

Horton, W., and I. Doxas, A low-dimensional energy-conserving state space model for substorm dynamics, *J. Geophys. Res., 101,* 27,223–27,237, 1996.

Horton, W., and I. Doxas, A low-dimensional dynamical model for the solar wind driven geotail-ionosphere system, *J. Geophys. Res., 103,* 4561–4572, 1998.

Klimas, A. J., D. N. Baker, D. A. Roberts, D. H. Fairfield, and J. Buchner, A nonlinear dynamical analogue model of geomagnetic activity, *J. Geophys. Res., 97,* 12,253-12,266, 1992.

Lorenz, E. N., Deterministic nonperiodic flow, *J. Atmos. Sci., 20,* 130–141, 1963.

Padhye, N., and W. Horton, Alfvén-wave particle interaction in finite-dimensional self-consistent field model, *Phys. Plasmas, 6,* 970–975, 1999.

Robinson, R.M., R.R. Vondrak, K. Miller, T. Dabbs, and D. Hardy, On calculating ionospheric conductances from the flux and energy of precipitating electrons, *J. Geophys. Res., 92,* 2565-2569, 1987.

Seydel, R., *Practical Bifurcation and Stability Analysis*, Springer-Verlag, New York, 1994.

Smith, J. P., Low-dimensional dynamics of the Earth's magnetosphere, Ph.D. thesis, Univ. of Tex. at Austin, May 1999.

Smith, J. P., and W. Horton, Analysis of the bimodal nature of solar wind-magnetosphere coupling, *J. Geophys. Res., 103,* 14,917–14,923, 1998.

Thiffeault, J-L, and W. Horton, Energy conserving truncations for convection with shear flow, *Phys. Fluids, 8,* 1715–1719, 1996.

Treve, Y. M., and O. P. Manley, Energy conserving Galerkin approximations for 2-D hydrodynamic and MHD Bénard convection, *Physica D, 4,* 319-342, 1982.

    J. P. Smith, J.-L. Thiffeault, W. Horton, Institute for Fusion Studies and Department of Physics, University of Texas at Austin, Austin, TX 78712-

1060. (e-mail: jpsmith@physics.utexas.edu, jeanluc@plasma.ap.columbia.edu, horton@physics.utexas.edu)

---

[1]Present address: Department of Applied Physics, Columbia University, New York, NY.
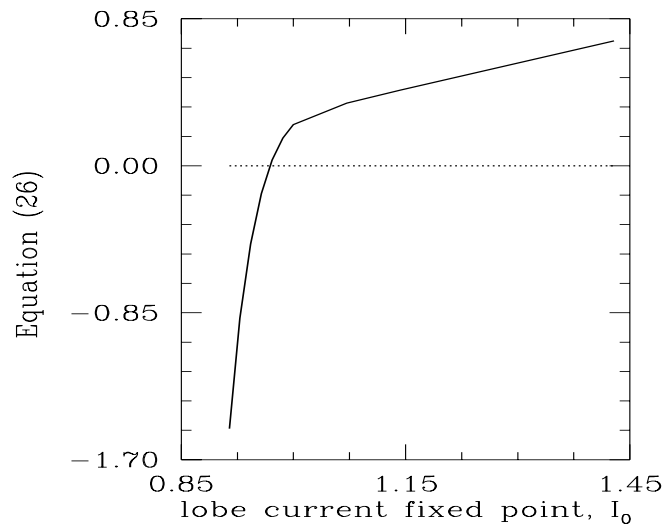
Figure 1. Equation for the roots of the lobe current.
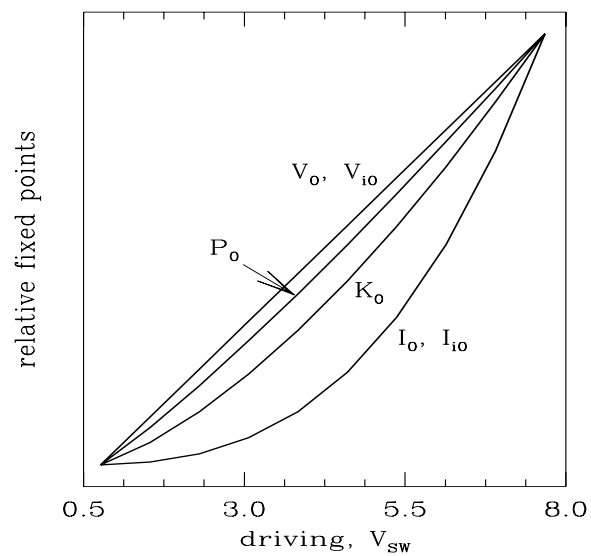
Figure 2. Relative values of the fixed points with respect to forcing for state S1.
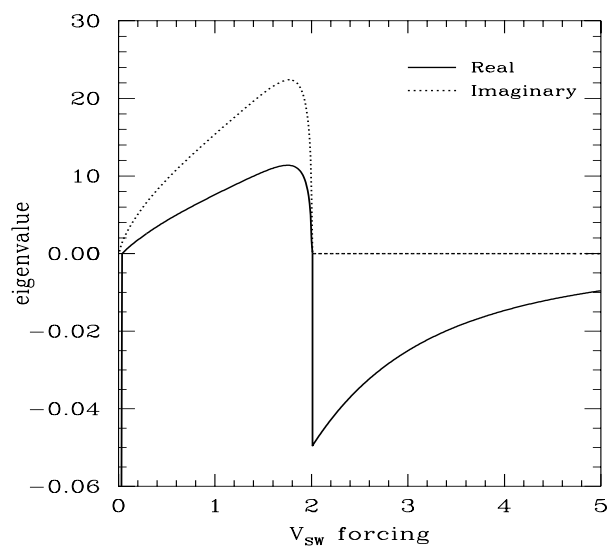
Figure 3. Eigenvalues with the largest real part for state S4 as a function of forcing V_{sw}. Note the different scales for the positive and negative y axes.
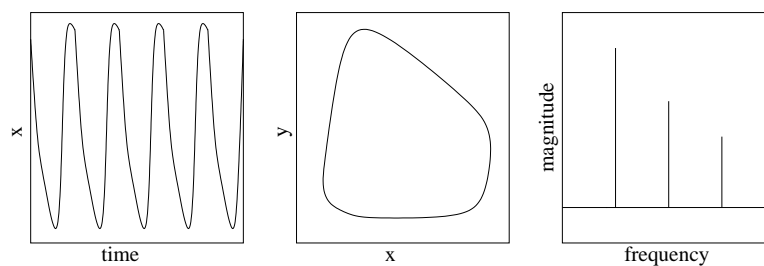
Figure 4. Example of a simple periodic limit cycle.
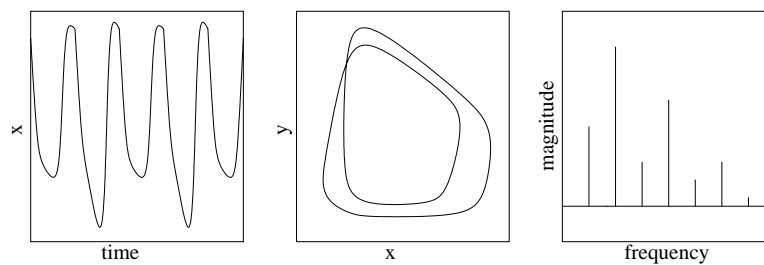
Figure 5. Period doubling of a limit cycle.
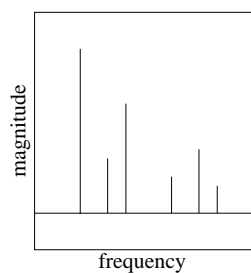
Figure 6. Spectrum for an irrational frequency torus. Note the two irrational primary frequencies.
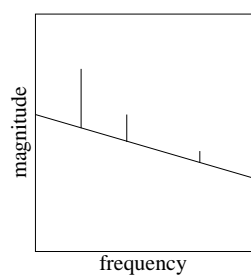
Figure 7. Spectrum for a chaotic attractor. The dominant feature is broadband noise.
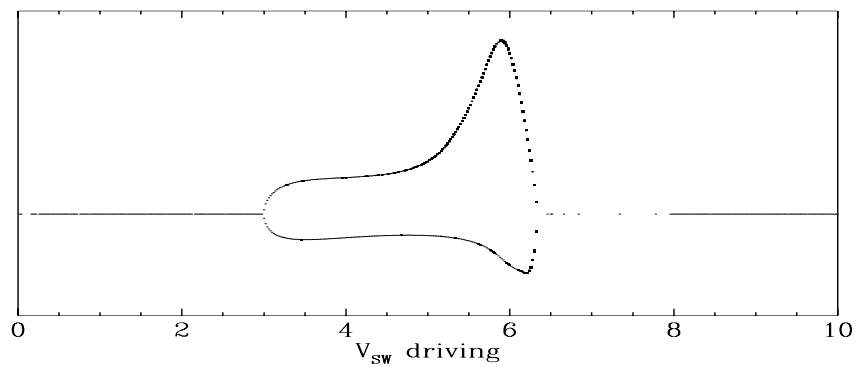
Figure 8. Bifurcation diagram for S2. See the end of section 5.2 for a discussion of the normalization of the vertical axis.
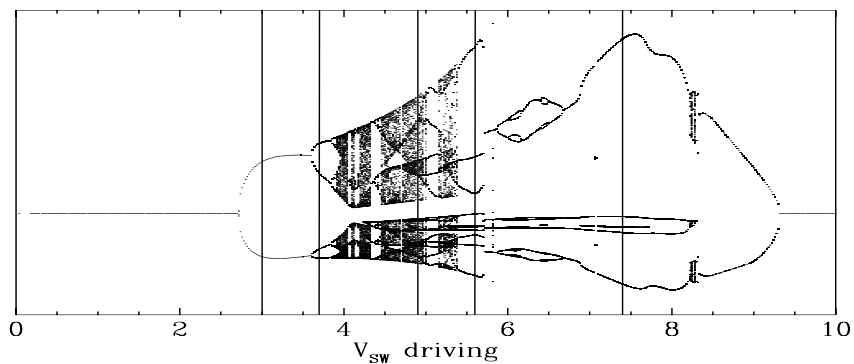
Figure 9. Bifurcation diagram for S3. The five vertical slices are shown in more detail in Figures 10–14. See the end of section 5.2 for a discussion of the normalization of the vertical axis.
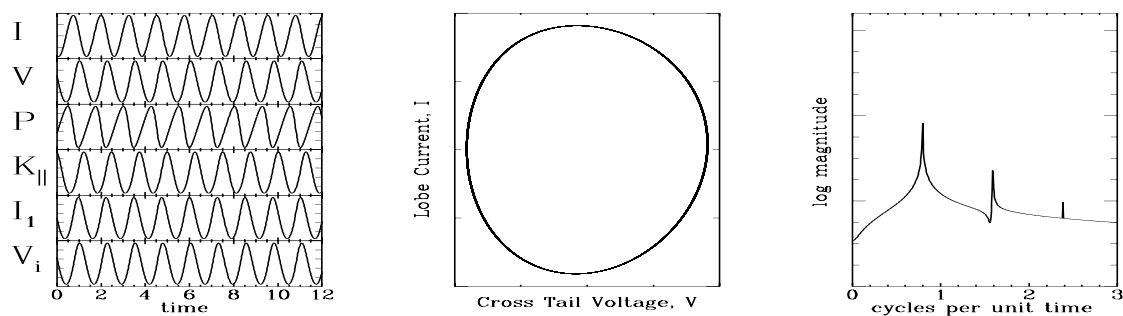
Figure 10. State S3 at $V_{\mathrm{sw}} = 3.0$.
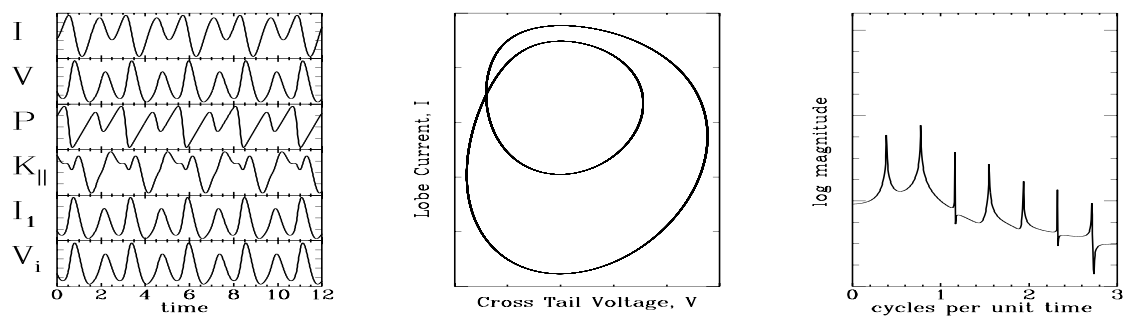
Figure 11. State S3 at $V_{\mathrm{sw}} = 3.7$. Note the period doubling from Figure 10.
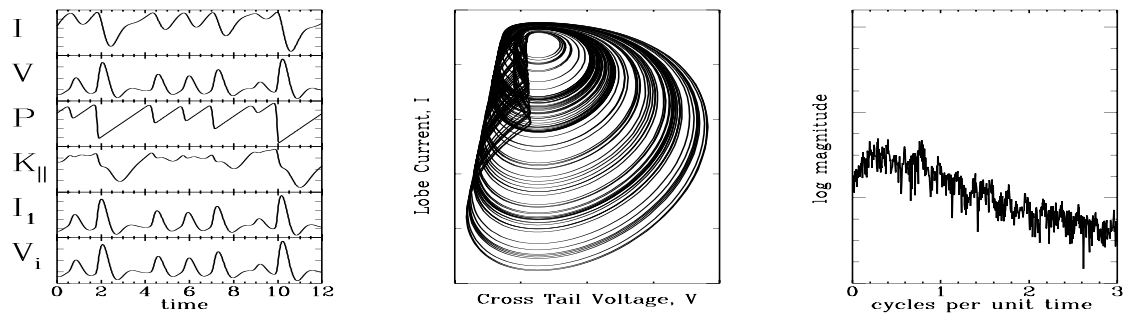
Figure 12. State S3 at $V_{\mathrm{sw}} = 4.91$.
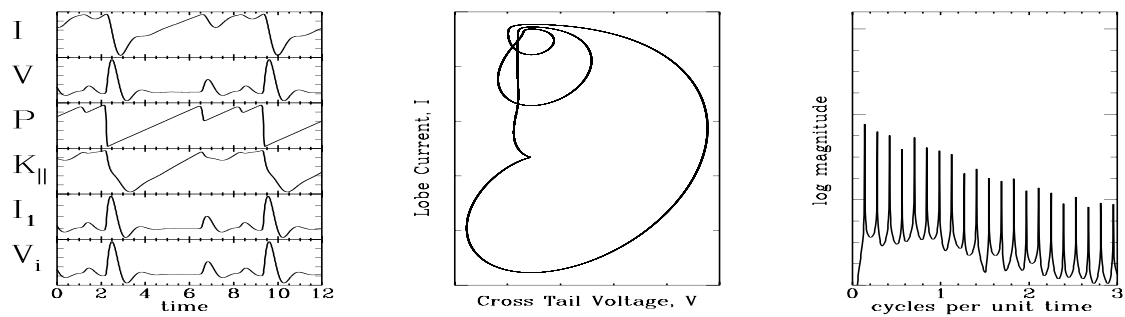
Figure 13. State S3 at $V_{\mathrm{sw}} = 5.6$.
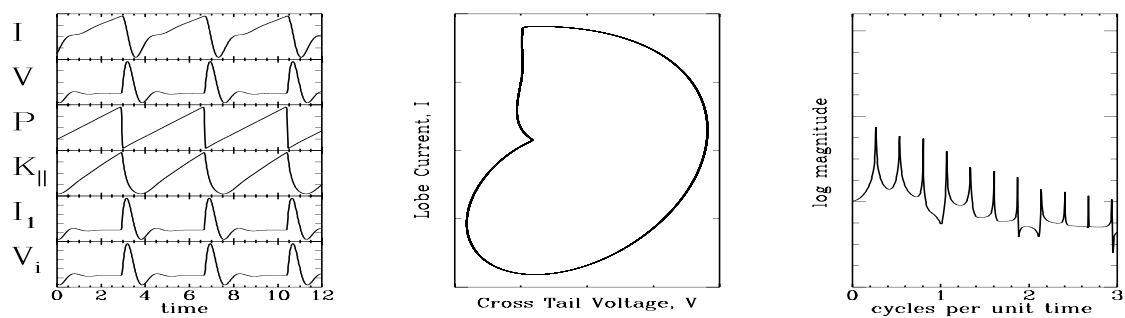
Figure 14. State S3 at $V_{\mathrm{sw}} = 7.4$.
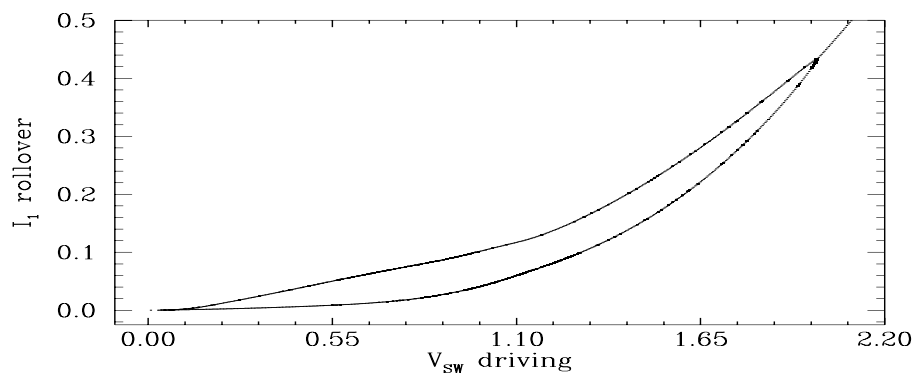
Figure 15. Bifurcation diagram for S4.
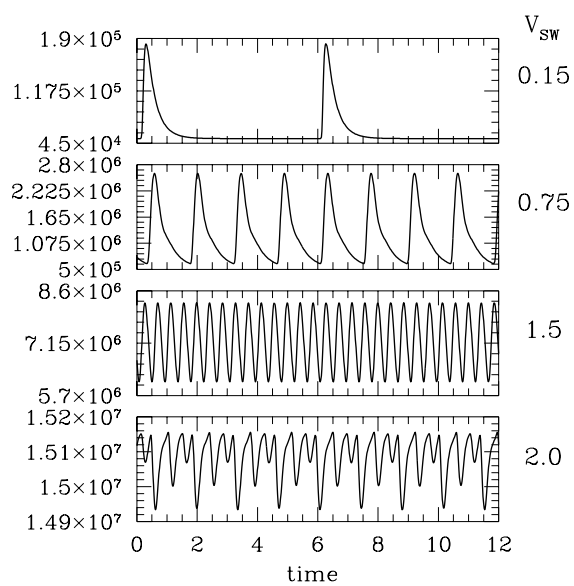
Figure 16. Ionospheric current for state S4 at different levels of forcing.

Table 1. Reference States in Dimension-less Coordinates

	S1	S2	S3	S4
a_1	0.0467	0.247	0.247	0.0467
a_2	0.00426	0.0391	0.391	0.00426
b_1	44.8	10.8	10.8	44.8
b_2	12.3	0.0752	0.0752	12.3
b_3	3.33	1.06	1.06	3.33
d_1	35	2200	2200	35,000
f_1	0.156	2.47	2.47	0.156
g_1	537	1080	1080	537
g_2	4	4	4	4
g_3	1210	37.9	3.79	121

Table 2. Fixed Points of the System in Dimensionless Coordinates for $V_{\text{sw}}=2$

	S1	S2	S3	S4
I_0	41.08	0.9975	0.9975	1.00007
V_0	2	2	2	2
P_0	2.297	12496.	12946.	2.316
K_0	3.031	223.6	227.6	3.044
I_{10}	40.51	0.0222	0.008319	0.4341
V_{i0}	2	2	2	2

Table A1. Dimensionless Reference States for Model Comparison. The values in parentheses in each column of this table correspond to the values in parentheses in the same column of Table A2, denoting where there are relationships between the dimensionless and the physical parameters.

	U1	U2	U3	U4	U5	U6	U7
a_1	1	1	1	1	1	1	1
a_2	0.9999	(0.95)	0.95	(0.05)	0.05	0.9999	0.9999
b_1	1	1	1	1	(10)	1	(10)
b_2	1	1	1	1	1	1	(10)
b_3	1	1	1	1	1	1	(10)
d_1	1	1	(1000)	1000	1	1	1
f_1	1	1	1	1	1	1	1
g_1	1	1	1	1	(10)	(10)	1
g_2	1	1	1	1	1	(10)	1
g_3	1	1	1	1	1	(10)	1

Table A2. Physical Reference States for Model Comparison. See caption of Table A1. Note that the units are the same as in Table A3 and were omitted for space reasons.

	U1	U2	U3	U4	U5	U6	U7
L	9230	(18.9)	18.9	(1.85)	(3.99)	9230	9230
C	542,000	542,000	542,000	542,000	(25,100)	542,000	(54,200)
Σ	542	542	542	542	(25.1)	542	542
L_1	9230	(18.9)	18.9	(1.85)	(3.99)	9230	9230
C_i	542,000	542,000	542,000	542,000	(25,100)	(54,200)	542,000
Σ_i	542	542	542	542	(25.1)	542	542
γ	0.371	0.371	0.371	0.371	(0.000545)	0.371	0.371
m	0.9999	(0.95)	0.95	(0.05)	0.05	0.9999	0.9999
I_c	1.84×10^7	1.84×10^7	1.84×10^7	1.84×10^7	1.84×10^7	1.84×10^7	1.84×10^7
ΔI	1.84×10^7	1.84×10^7	(1.84×10^4)	1.84×10^4	1.84×10^7	1.84×10^7	1.84×10^7
u_0	6×10^{-11}	6×10^{-11}	6×10^{-11}	6×10^{-11}	(1.29×10^{-10})	6×10^{-11}	6×10^{-11}
$\tau_\parallel$	1×10^3	1×10^3	1×10^3	1×10^3	1×10^3	1×10^3	1×10^3
α	1.14×10^{12}	1.14×10^{12}	1.14×10^{12}	1.14×10^{12}	(2.46×10^{11})	1.14×10^{12}	1.14×10^{12}
Ω	1.6×10^{24}	1.6×10^{24}	1.6×10^{24}	1.6×10^{24}	1.6×10^{24}	1.6×10^{24}	1.6×10^{24}

Table A3. Reference States of the WINDMI Model (in Physical Coordinates)

	S1	S2	S3	S4	Units
L	40	10	10	40	H
C	12,000	5×10^4	5×10^4	12,000	F
Σ	40	53	53	40	mho
L_1	12	1	1	12	H
C_i	1000	500	500	1000	F
Σ_i	4	2	2	4	mho
γ	8×10^{-4}	2×10^{-5}	$<2\times10^{-6}$	8×10^{-5}	mho$/\sqrt{AV}$
m	0.05	0.5	0.5	0.05	
I_c	35×10^6	22×10^6	22×10^6	35×10^6	A
ΔI	1×10^6	1×10^4	1×10^4	1×10^3	A
u_0	6×10^{-11}	6×10^{-10}	6×10^{-10}	6×10^{-11}	J$^{-1/2}$ s^{-1}
$\tau_\parallel$	1000	1000	1000	1000	s
α	1.14×10^{12}	8×10^{10}	8×10^{10}	1.14×10^{12}	$C/Pa^{0.5}$
Ω	1.6×10^{24}	1.6×10^{25}	1.6×10^{25}	1.6×10^{24}	m^3

Table A4. Fixed Points of the System (in Physical Coordinates) for V_{sw}=100 kV. Note the difference of 25 orders of magnitude between P_0 and K_0.

	S1	S2	S3	S4
I_0, A	6.57×10^8	2.20×10^7	2.20×10^7	3.50×10^7
V_0, V	1×10^5	1×10^5	1×10^5	1×10^5
P_0, Pa	1.18×10^{-10}	3.95×10^{-8}	4.21×10^{-8}	4.37×10^{-10}
K_0, J	1.24×10^{15}	1.59×10^{15}	1.64×10^{15}	2.38×10^{15}
I_{10}, A	6.41×10^8	746000	230000	7.18×10^6
V_{i0}, V	1×10^5	1×10^5	1×10^5	1×10^5